

ORFormer: Occlusion-Robust Transformer for Accurate Facial Landmark Detection

Jui-Che Chiang^{1,3} Hou-Ning Hu² *Bo-Syuan Hou¹ *Chia-Yu Tseng¹
 Yu-Lun Liu¹ Min-Hung Chen³ Yen-Yu Lin¹

¹National Yang Ming Chiao Tung University ²MediaTek Inc. ³NVIDIA

<https://ben0919.github.io/ORFormer>

Abstract

Although facial landmark detection (FLD) has gained significant progress, existing FLD methods still suffer from performance drops on partially non-visible faces, such as faces with occlusions or under extreme lighting conditions or poses. To address this issue, we introduce ORFormer, a novel transformer-based method that can detect non-visible regions and recover their missing features from visible parts. Specifically, ORFormer associates each image patch token with one additional learnable token called the messenger token. The messenger token aggregates features from all but its patch. This way, the consensus between a patch and other patches can be assessed by referring to the similarity between its regular and messenger embeddings, enabling non-visible region identification. Our method then recovers occluded patches with features aggregated by the messenger tokens. Leveraging the recovered features, ORFormer compiles high-quality heatmaps for the downstream FLD task. Extensive experiments show that our method generates heatmaps resilient to partial occlusions. By integrating the resultant heatmaps into existing FLD methods, our method performs favorably against the state of the arts on challenging datasets such as WFLW and COFW.

faces caused by occlusions, extreme lighting conditions, or extreme head rotations, because the features extracted from non-visible regions are corrupted. An FLD method with non-visible region detection and reliable feature extraction is in demand.

In this work, we introduce an occlusion-robust transformer, called *ORFormer*, which can identify non-visible regions and recover their missing features, and is applied to generate high-fidelity heatmaps resilient to challenging scenarios. As illustrated in Figure 1, our ORFormer builds on Vision Transformer [5], where image patch tokens interact with each other via the self-attention mechanism. For non-visible part detection, we associate each patch token X_i with an extra learnable token M_i called *messenger token*.

The messenger token M_i simulates occlusion present in patch i and aggregates features from all patch tokens except X_i . Subsequently, our occlusion detection module accesses the disparity between the regular patch embedding X'_i and the messenger embedding M'_i to determine if occlusion is present in patch i . For occlusion handling, our feature recovery module recovers the missing features of the occluded patch by a convex combination of X'_i and M'_i with the combination coefficient predicted by the occlusion detection module. The resulting features are then utilized to generate heatmaps, and our proposed mechanism makes the output heatmaps remain robust in extreme scenarios.

We integrate the high-quality heatmaps generated by ORFormer as complementary information into existing landmark detection methods [11, 47]. Our method achieves state-of-the-art performance on multiple benchmark datasets, including WFLW [40] and COFW [3], showcasing the robustness of our method in handling partially non-visible faces.

The main contributions of this work are summarized as follows: First, we present a novel occlusion-robust transformer, ORFormer, which utilizes the proposed learnable messenger token to simulate potential occlusions and recover missing features. ORFormer enables a transformer

1. Introduction

Facial landmark detection (FLD) aims to localize specific key points on human faces, such as those on eyes, noses, and mouths. It is pivotal for numerous downstream applications, such as face recognition [13, 29], facial expression recognition [1, 25], head pose estimation [10, 33], and augmented reality [14, 38]. Recent advances in deep neural networks have significantly enhanced facial landmark detection [7, 8, 11, 36, 42, 47]. However, existing FLD methods suffer from performance drops on partially non-visible

*means equal contribution

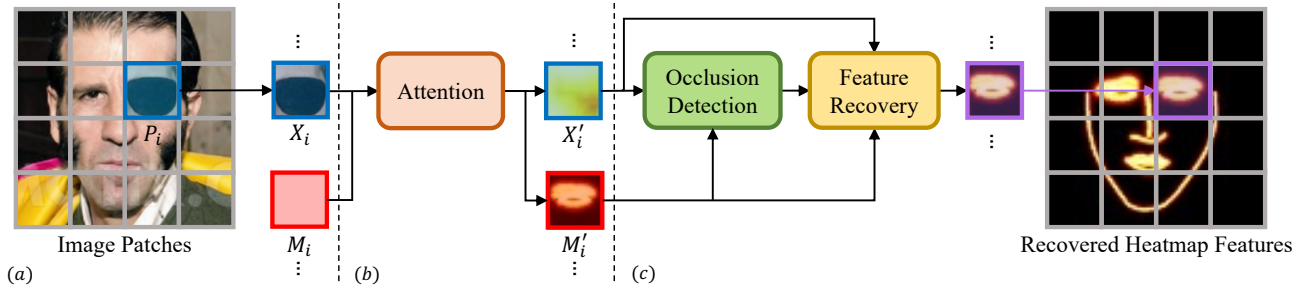


Figure 1. **Overview of our ORFormer.** (a) For each patch P_i , we introduce a patch token X_i and a learnable messenger token M_i for occlusion detection and handling. (b) The messenger token computes attention with patch tokens other than its corresponding one. (c) We detect occlusion by evaluating the dissimilarity between the regular embedding X'_i and the messenger embedding M'_i , and then recover occluded features based on the messenger embedding which is aggregated from other image patches, if occlusion is present in patch P_i .

to detect and handle non-visible tokens in a general way. Second, our ORFormer is applied for robust heatmap generation, thereby enhancing the applicability of existing FLD methods to partially non-visible faces. Third, our method performs favorably against state-of-the-art facial landmark detection methods on two challenging datasets, WFLW and COFW, showcasing its robustness to extreme cases

2. Related Work

2.1. Facial Landmark Detection

Most FLD methods rely on coordinate regression and/or heatmap regression. The former directly estimates the landmark coordinates of a face. The latter predicts a heatmap for each landmark and completes FLD with post-processing.

Coordinate Regression. Some methods [7, 8, 23, 40, 44, 45] employ linear layers as decoders to regress landmarks from CNN features. Feng *et al.* [7] design a new loss function for improved landmark supervision. Wu *et al.* [40] utilize facial contours to impose constraints on landmark supervision while providing a dataset with various extreme cases. Miao *et al.* [23] proposed Fourier feature pooling to handle highly nonlinear relationships between images and facial shapes. These methods offer end-to-end trainable solutions.

To leverage the self-attention mechanism in Transformer [35] for facial structures exploration, some studies [18–20, 37, 39, 42] utilize the transformer decoder to learn the mapping between CNN features and landmarks. Xia *et al.* [42] propose a coarse-to-fine decoder focusing on sparse local patches. Li *et al.* [19] learn landmark queries along pyramid CNN features. However, linear layers in CNN and global feature dependence in transformers are sensitive to partial occlusions.

Heatmap Regression. Inspired by the advances in heatmap generation [26, 30, 32], some studies [2, 4, 16, 26, 27,

36] integrate heatmap regression into facial landmark detection. They convert landmark annotations to heatmaps for model supervision. Kumar *et al.* [16] estimate uncertainty and visibility likelihood with heatmaps for stable model convergence. Newell *et al.* [26] employ a stacked hour-glass network with intermediate heatmap supervision and utilize Argmax operator to obtain landmarks. However, Argmax in heatmap regression limits direct supervision by landmarks due to its non-differentiable nature.

Recent studies, such as replacing Argmax with other differential decoders, enable heatmap regression methods to be end-to-end trainable and supervised by both heatmaps and landmarks. For example, Jin *et al.* [12] reduce heatmap regression to confidence score and offset prediction to avoid heavy upsampling layers and the use of Argmax. With the aid of differential decoders, Huang *et al.* [11] and Zhou *et al.* [47] design new loss functions with both landmark and heatmap supervision to alleviate the negative impact caused by landmark annotation ambiguities. Micaelli *et al.* [24] utilize the deep equilibrium model to compute cascaded landmark refinement. The capability of heatmap regression methods that can be supervised by both landmarks and heatmaps while preserving facial structures has propelled them to the state-of-the-art status.

However, the aforementioned coordinate regression and heatmap regression methods are vulnerable to faces with partial occlusions, under extreme lighting conditions, or in extreme head rotations due to feature occlusion and corruption.

2.2. Occlusion-Robust Facial Landmark Detection

We discuss three major categories of methodologies for occlusion-robust facial landmark detection as follows:

Methods in the first category such as [16, 20, 26, 41] estimate the probability of occlusion occurrence for each landmark and alleviate the negative impact of corrupted features computed in occluded areas. For example, Kumar *et al.* [16] and Li *et al.* [20] propose joint landmark location, uncer-

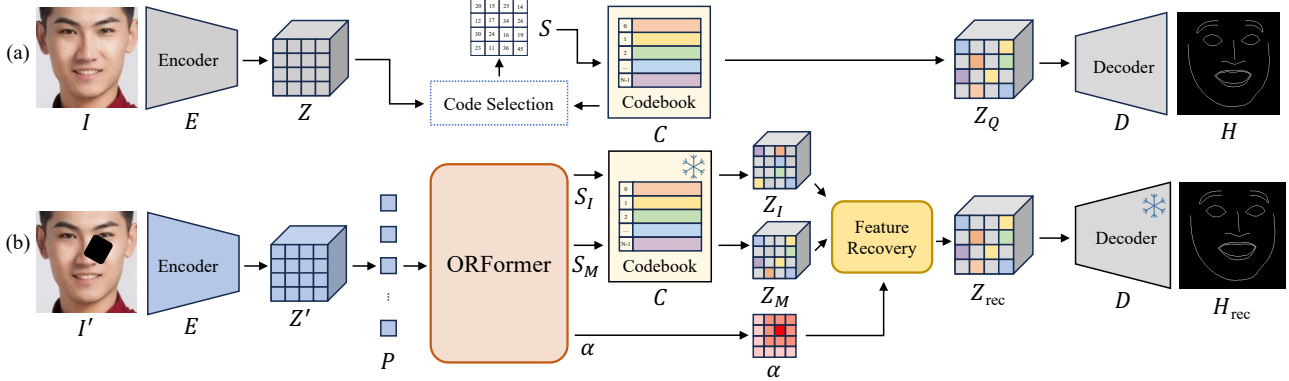


Figure 2. **Overview of our method.** (a) We first train a quantized heatmap generator, which takes an image I as input and generates its edge heatmaps H . After pre-training, the prior knowledge of unoccluded faces is encoded in the codebook C and decoder D . (b) With the frozen codebook and decoder, we introduce ORFormer to generate the occlusion map α and two code sequences S_I and S_M , leading to quantized features Z_I and Z_M . The recovered feature Z_{rec} is yielded by merging Z_I and Z_M with patch-specific weights given in α , and is used to produce occlusion-robust heatmaps H_{rec} .

tainty, occlusion probabilities, and/or visibility prediction. However, these methods rely on additional annotations indicating whether a landmark is occluded or not, while our method does not require these annotations.

The second category explores the consensus among image patches to identify occluded ones. For example, Burgos-Artizzu *et al.* [3] propose a method that enforces regressors focusing on different image patches to reach a consensus, trusting those using local features from non-occluded areas. While their method and ours share a similar concept, their method ignores the occluded features without recovering them, restricting the ability of occluded landmark detection. In contrast, we propose the messenger token, which aggregates information from non-occluded areas and enables feature recovery for occluded patches.

The third category utilizes global context to deal with occlusions. Merget *et al.* [22] introduce global context directly into a fully convolutional neural network. Zhu *et al.* [49] propose a geometry-aware module to excavate geometric relationships between different facial components, while Zhu *et al.* [48] model the hierarchies between facial components. However, these works do not explicitly detect the occluded areas and therefore do not recover features for these areas, being suboptimal for significant occlusions.

2.3. Transformer for Feature Recovery

Transformers [5, 35] have been widely adopted in vision tasks. Transformers leverage attention mechanisms to capture long-range dependencies between tokens, but are sensitive to feature corruption or partial occlusions.

To address this issue, Xu *et al.* [43] utilize cross-attention to recover occluded features between different frames in the context of object re-identification. However, their method

relies on multiple frames, whereas our approach focuses on recovering occluded features within a single image. Park *et al.* [28] proposes a method for 3D hand mesh estimation that involves training a CNN block to separate primary and secondary features, followed by utilizing cross-attention to recover occluded features. In contrast, our method integrates occlusion detection and handling mechanisms into a single transformer, enabling adaptive detection and recovery of occluded features within a single frame.

Zhou *et al.* [46] pre-train a quantized autoencoder [6], employ a ViT model [5], and utilize self-attention to recover corrupted features for blind face restoration. While their approach shares similarities with ours, relying on self-attention with partially corrupted features may fail since attention values of the occluded tokens cannot be faithfully computed. To alleviate this issue, we develop messenger tokens and present a module to adaptively combine the regular and messenger embeddings for feature recovery.

3. Proposed Method

The section presents ORFormer, a general method that can be integrated into a regular transformer for occlusion detection and handling. Figure 2 illustrates our method. Firstly, we adopt the concept of vector quantization [34], similar to the approach in Codeformer [46], and pre-train a quantized heatmap generator (Section 3.1). Subsequently, the learned discrete codebook and decoder are employed as a prior for heatmap generation. Leveraging this learned prior, we utilize ORFormer for code sequence prediction and feature recovery for the partially occluded image patches (Section 3.2). Lastly, with the aid of ORFormer, we integrate our heatmaps generated from recovered features into the existing FLD methods (Section 3.3).

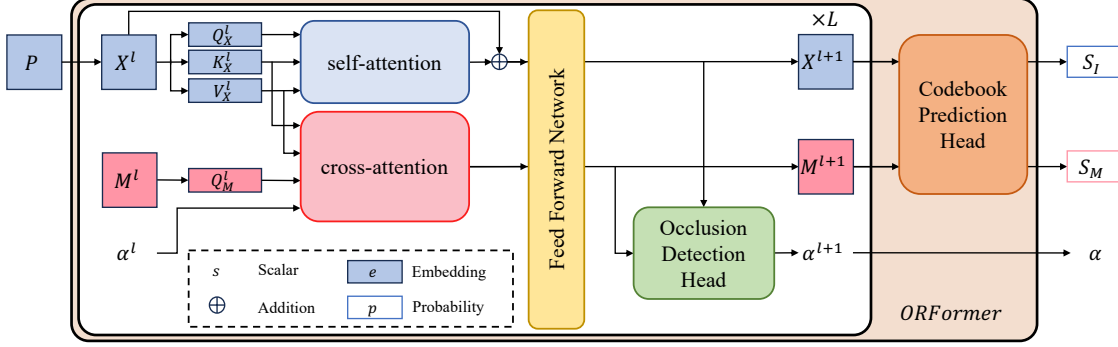


Figure 3. **Network architecture of ORFormer.** ORFormer takes image patches P as input and generates two code sequences S_I and S_M via the codebook prediction head. While S_I is computed by referring to the image patch tokens, S_M is by the messenger tokens. The occlusion map α represents the patch-specific occlusion likelihood and is inferred by the occlusion detection head.

3.1. Quantized Heatmap Generator

To enhance robustness against occlusions during heatmap generation, we include the training of a quantized heatmap generator. By training this generator on faces without occlusions, we can learn a high-dimensional latent space tailored explicitly for heatmap generation under ideal conditions. With the learned codebook, we reduce uncertainty in restoring occluded features, as the code items are learned from non-occluded faces.

As illustrated in Figure 2(a), an unoccluded face image $I \in \mathbb{R}^{h \times w \times 3}$ is encoded into the latent space $Z \in \mathbb{R}^{m \times n \times d}$ by an encoder E . Following the principles in VQVAE [34], each patch $Z^{i,j}$ in the encoded features Z is replaced with the nearest dictionary item, *i.e.*, code, in the learnable codebook $C = \{c_s \in \mathbb{R}^d\}_{s=0}^{N-1}$ of N codes to obtain the quantized feature $Z_Q \in \mathbb{R}^{m \times n \times d}$ and its corresponding code index sequence $S \in \{0, 1, \dots, N-1\}^{h \times w}$, *i.e.*,

$$\begin{aligned} Z_Q^{i,j} &= \arg \min_{c_s \in C} \|Z^{i,j} - c_s\|_2 \text{ and} \\ S^{i,j} &= \arg \min_s \|Z^{i,j} - c_s\|_2. \end{aligned} \quad (1)$$

Subsequently, the decoder D generates the edge heatmaps $H \in \mathbb{R}^{h \times w \times N_E}$ based on the quantized feature Z_Q , where N_E is the number of edges (facial contours) per face. In this work, we adopt the same edge heatmap definition as that in [40].

Loss Functions. To train the quantized heatmap generator with a learnable codebook, we utilize an image-level loss \mathcal{L}_{img} . In addition, we incorporate an intermediate latent space loss $\mathcal{L}_{\text{latent}}$ to minimize the distance between the codebook C and the encoded feature Z . These loss functions are defined by

$$\begin{aligned} \mathcal{L}_{\text{img}} &= \|H - \hat{H}\|_2^2 \text{ and} \\ \mathcal{L}_{\text{latent}} &= \|\text{sg}(Z) - Z_Q\|_2^2 + \beta \|Z - \text{sg}(Z_Q)\|_2^2, \end{aligned} \quad (2)$$

where \hat{H} is the ground-truth edge heatmaps, $\text{sg}(\cdot)$ stands for the stop-gradient operator, and β is a hyper-parameter used for loss balance. The complete loss function for learning the codebook heatmap generator $\mathcal{L}_{\text{codebook}}$ is given by

$$\mathcal{L}_{\text{codebook}} = \mathcal{L}_{\text{img}} + \lambda_{\text{latent}} \cdot \mathcal{L}_{\text{latent}}, \quad (3)$$

where λ_{latent} is a hyper-parameter used for loss balance.

3.2. ORFormer

Given an occluded or partially non-visible face as input, conventional nearest-neighbor searching described in (1) may fail on the occluded patches due to their feature corruption. However, relying solely on self-attention in transformers, *e.g.* [46], is insufficient in heatmap generation since the attention map calculated with corrupted features no longer faithfully captures the relationships between patches. To this end, we propose ORFormer to detect occluded patches and recover their features.

As shown in Figure 2(b), we introduce the proposed ORFormer after training the heatmap generator. ORFormer takes as input image patches $P = \{P_k\}_{k=0}^{m \times n - 1}$ from the features Z' , which are extracted by the encoder E . ORFormer employs both regular and messenger tokens for computing patch features. It generates the patch-specific occlusion map $\alpha \in \mathbb{R}^{m \times n}$ and two code sequences, $S_I \in \{0, 1, \dots, N-1\}^{m \times n}$ and $S_M \in \{0, 1, \dots, N-1\}^{m \times n}$. While S_I is computed from regular tokens and brings information from all patches, S_M is derived from messenger tokens and is occlusion-aware. Based on the codes in S_I and S_M , quantized features Z_I and Z_M are produced by referring to codebook C . Z_I and Z_M are merged by based on the occlusion map α in a patch-specific manner, and form the recovered feature Z_{rec} . Finally, Z_{rec} along with the pre-trained decoder is used to generate the heatmaps H_{rec} .

We freeze the codebook C and decoder D after the pre-training stage while fine-tuning the encoder E to facilitate

heatmap generation under feature occlusion. The proposed ORFormer, shown in Figure 3, is elaborated as follows:

Self-attention. As shown in Figure 3, ORFormer is a transformer with L layers. At each layer l , it computes self-attention among regular image patch tokens by

$$X^{l+1} = \text{FFN}\{\text{softmax}(Q_X^l (K_X^l)^\top) V_X^l + X^l\}, \quad (4)$$

where queries Q_X^l , keys K_X^l , and values V_X^l are obtained from patch tokens X^l through linear embeddings. Residual learning [9] and a feed-forward network (FFN) are employed here.

Cross-attention. In addition to conventional self-attention between image patch tokens, we introduce the messenger tokens, denoted as M^l , one for each patch. The messenger tokens are designed to simulate feature occlusion. As shown in Figure 3, we only compute their queries Q_M^l , each of which is used to aggregate features from all but its corresponding patch token via cross-attention:

$$M^{l+1} = \text{FFN}\{\text{softmax}(A_{\text{cross}}(Q_M^l, K_X^l)) V_X^l\}, \quad (5)$$

where

$$A_{\text{cross}}(Q_M^l, K_X^l)^{i,j} = \begin{cases} 0, & \text{if } i = j, \\ (Q_M^l (K_X^l)^\top)^{i,j}, & \text{otherwise.} \end{cases} \quad (6)$$

(6) computes the cross-attention score between the i -th messenger token and the j -th image patch token. By excluding features from the corresponding patch, the resultant messenger tokens M^{l+1} encode features borrowed from other image tokens, simulating feature occlusion.

Occlusion Detection Head. Following the attention mechanism and the feed-forward network, we derive an occlusion detection head to detect occluded patches by referring to the dissimilarity between the image patch embedding X^{l+1} and the messenger embedding M^{l+1} . A patch-specific occlusion map $\alpha^{l+1} = \{\alpha_k^{l+1}\}_{k=0}^{m \times n - 1}$ is obtained:

$$\alpha_k^{l+1} = \sigma(W^{l+1} \cdot \text{dist}(X_k^{l+1}, M_k^{l+1})), \quad (7)$$

where the function $\text{dist}(\cdot, \cdot)$ computes the element-wise squared difference between the two embeddings. W^{l+1} is a fully connected layer transforming the embedding returned by dist into a scalar. $\sigma(\cdot)$ is the sigmoid function ensuring α_k^{l+1} ranges between 0 and 1. Higher α_k^{l+1} indicates that patch k is more likely to be occluded.

Occlusion-aware Cross-attention. After obtaining the occlusion map $\alpha^l \in \mathbb{R}^{m \times n}$ at the $(l-1)$ -th layer, the messenger tokens at the l -th layer are allowed to suppress feature aggregation from occluded patches. Specifically, the

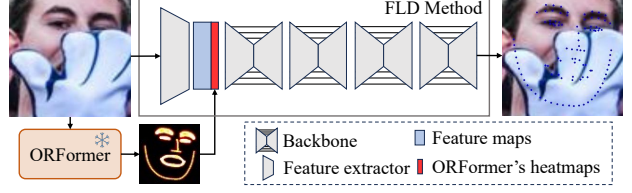


Figure 4. **Integration of ORFormer into an existing FLD method.** ORFormer is adopted for occlusion detection and feature recovery, resulting in high-quality heatmaps. The generated heatmaps serve as an extra input to an FLD method, and offer the recovered features to make the FLD method robust to occlusions.

cross-attention adopted by messenger tokens in (6) is modified to

$$A_{\text{cross}}(Q_M^l, K_X^l)^{i,j} = \begin{cases} 0, & \text{if } i = j, \\ (1 - \alpha_j^l) (Q_M^l (K_X^l)^\top)^{i,j}, & \text{otherwise.} \end{cases} \quad (8)$$

Since α_j^l gives the likelihood of occlusion occurrence in the j -th image patch, the coefficient $(1 - \alpha_j^l)$ in (8) prevents a messenger token from aggregating features from patch j with a larger value of α_j^l . At the first layer, the initial occlusion map α^1 is set to 0. At the last layer, *i.e.*, the L -th layer, the resultant occlusion map α^{L+1} will be used in the following step for feature recovery, and is denoted as α for simplicity in Figure 2(b).

Feature Recovery. In Figure 3, the image embedding X^{L+1} and the messenger embedding M^{L+1} produced in the last layer of ORFormer are fed into a codebook prediction head. This head predicts the code sequence $S_I \in \{0, 1, \dots, N-1\}^{m \times n}$ based on the image embedding X^{L+1} , where each entry in S_I searches the code index for its corresponding patch via (1). The quantized features $Z_I \in \mathbb{R}^{m \times n \times d}$ are produced by retrieving the corresponding $m \times n$ code items from the codebook C . Similarly, the other code sequence S_M and quantized features Z_M are generated based on the messenger embedding M^{L+1} .

The quantized features Z_I and Z_M store complementary information. While Z_I considers all patches but is sensitive to corrupted features, Z_M focuses on non-occluded patches but ignores the original patch features P as shown in Figure 3. We use the predicted occlusion map $\alpha \in \mathbb{R}^{m \times n}$ to recombine the final recovered features $Z_{\text{rec}} \in \mathbb{R}^{m \times n \times d}$ by merging Z_I and Z_M in a patch-specific manner, *i.e.*,

$$Z_{\text{rec}} = (1 - \alpha) \otimes Z_I + \alpha \otimes Z_M, \quad (9)$$

where $A \otimes B$ denotes element-wise multiplication between A and B along the third dimension of B .

Loss Functions. After the pre-training stage, we learn the ORFormer and fine-tune the encoder E while keeping the

Method	Backbone	WFLW-Full			COFW		300W (NME↓)		
		NME↓	FR↓	AUC↑	NME↓	Full	Comm.	Chal.	
LAB [40]	Hourglass	5.27	7.56	0.532	-	3.49	2.98	5.19	
Wing [7]	ResNet-50	4.99	6.00	0.550	5.44	-	-	-	
HRNet [32]	HRNet-W18	4.60	4.64	-	-	3.32	2.87	5.15	
AWing [36]	Hourglass	4.36	2.84	0.572	4.94	3.07	2.72	4.52	
LUVLi [16]	DU-Net	4.37	3.12	0.577	-	3.23	2.76	5.16	
ADNet [11]	Hourglass	4.14	2.72	0.602	4.68	2.93	2.53	4.58	
PIPNet [12]	ResNet-101	4.31	-	-	-	3.19	2.78	4.89	
HIH [17]	Hourglass	4.08	2.60	0.605	4.63	3.09	2.65	4.89	
SLPT [42]	HRNet-W18	4.14	2.76	0.595	4.79	3.17	2.75	4.90	
RePFormer [19]	ResNet-101	4.11	-	-	-	3.01	-	-	
†STAR [47]	Hourglass	4.03	2.32	0.611	4.62	2.90	2.52	4.46	
LDEQ [24]	Hourglass	3.92	2.48	0.624	-	-	-	-	
ORFormer (Ours)	Hourglass	3.86	1.76	0.622	4.46	2.90	2.53	4.43	

Table 1. **Quantitative comparison with state-of-the-art methods on WFLW, COFW, and 300W.** NME is reported for all datasets. For WFLW, FR and AUC with a threshold of 10% are included. The **best** and **second best** results are highlighted. The † symbol represents the results we reproduced.

codebook C and the decoder D fixed. We employ the cross-entropy loss for code sequence prediction $\mathcal{L}_{\text{code}}$ on both S_I and S_M via

$$\mathcal{L}_{\text{code}}(\hat{S}) = \sum_{k=0}^{m \times n - 1} -S_k \log(\hat{S}_k), \quad (10)$$

where $\hat{S} \in \{S_I, S_M\}$ and the ground truth of the code sequence S is obtained from the pre-trained heatmap generator mentioned in Section 3.1. We also employ image-level loss \mathcal{L}_{img} given in (2) between H_{rec} and \hat{H} . The complete loss function for learning ORFormer $\mathcal{L}_{\text{ORFormer}}$ is

$$\mathcal{L}_{\text{ORFormer}} = \mathcal{L}_{\text{code}}(S_I) + \mathcal{L}_{\text{code}}(S_M) + \lambda_{\text{img}} \cdot \mathcal{L}_{\text{img}}, \quad (11)$$

where λ_{img} is a hyper-parameter used for loss balance.

3.3. Integration with FLD Methods

With our ORFormer for occlusion detection and feature recovery, the quantized heatmap generator can produce high-quality heatmaps. To evaluate the effectiveness of the output heatmaps, we integrate them as additional structural guidance into existing FLD methods [11, 47]. As illustrated in Figure 4, the integration involves merging the heatmaps produced by the heatmap generator and the feature maps yielded by an existing FLD method. Specifically, we concatenate the heatmaps with the feature maps in the early stage and merge them with a single lightweight CNN block. Utilizing the merged features, our proposed method can model a more robust facial structure and enhance the performance of existing FLD methods, especially on occluded or partially non-visible faces.

4. Experiments

4.1. Experimental Settings

Implementation Details. The quantized heatmap generator takes images of resolution $64 \times 64 \times 3$ as input and out-

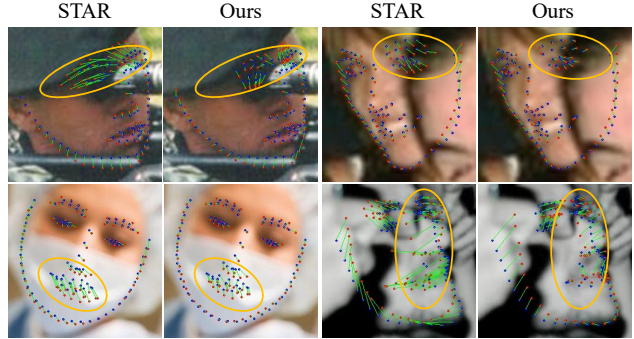


Figure 5. **Qualitative comparison with the reproduced baseline method, STAR, on extreme cases from the test set of WFLW.** The ground-truth landmarks are marked in blue, while the predicted landmarks are in red. The green lines represent the distance between the ground-truth landmarks and the predicted landmarks. Orange ellipses highlight variations between the methods in the challenging areas.

puts $64 \times 64 \times N_E$ heatmaps, where N_E is the number of edges per face. Its latent space size is $m \times n \times d$, and the codebook size is $N \times d$, where N is the number of code entries, and each entry is a d -dimensional vector. The ORFormer is a 3-layer transformer structure operating within the latent space of the quantized heatmap generator. Its token size is set to $1 \times 1 \times d$ with a total of $m \times n$ tokens. We empirically set m and n to 16, d to 256, and N to 2,048.

For the landmark detection models, we follow the same setup as ADNet [11] and STAR [47]. We use a four-stacked hourglass network [26] as the backbone. Each hourglass outputs feature maps of resolution 64×64 . To incorporate the output heatmaps from ORFormer into the feature maps, we concatenate them and then apply a 1×1 convolutional block to merge them before the first hourglass block. We train the model from scratch only on the target dataset without external data or pre-trained weights. For the loss balance hyper-parameters, we empirically set β to 0.25, λ_{latent} to 100, and λ_{img} to 50.

Datasets. We conducted experiments on three public datasets: WFLW [40], COFW [3], and 300W [31].

WFLW is widely recognized as the standard benchmark in facial landmark detection, containing 7,500 training images and 2,500 testing images, with 98 landmarks per image. This dataset presents significant challenges due to its diverse range of extreme cases, including variations in pose, expression, illumination, makeup, occlusion, and blur. Each sample in the dataset is accompanied by additional labels indicating the specific extreme case it represents.

COFW is a benchmark with 1,345 training images and 507 testing images, with 29 landmarks per image. This dataset is known for face occlusion, with an average of 23%

Method	BackBone	NME \downarrow						
		Full	Pose	Exp.	Ill.	Mak.	Occ.	Blur
LAB [40]	Hourglass	5.27	10.24	5.51	5.23	5.15	6.79	6.12
Wing [7]	ResNet-50	4.99	8.43	5.21	4.88	5.26	6.21	5.81
HRNet [32]	HRNet-W18	4.60	7.94	4.85	4.55	4.29	5.44	5.42
AWing [36]	Hourglass	4.36	7.38	4.58	4.32	4.27	5.19	4.96
ADNet [11]	Hourglass	4.14	6.96	4.38	4.09	4.05	5.06	4.79
PIPNet [12]	ResNet-101	4.31	7.51	4.44	4.19	4.02	5.36	5.02
HIH [17]	Hourglass	4.08	6.87	4.06	4.34	3.85	4.85	4.66
SLPT [42]	HRNet-W18	4.14	6.96	4.45	4.05	4.00	5.06	4.79
RePFormer [19]	ResNet-101	4.11	7.25	4.22	4.04	3.91	5.11	4.76
†STAR [47]	Hourglass	4.03	6.78	4.26	3.97	3.85	4.82	4.59
LDEQ [24]	Hourglass	3.92	6.86	3.94	4.17	3.75	4.77	4.59
ORFormer (Ours)	Hourglass	3.86	6.63	4.13	3.83	3.61	4.57	4.50

Table 2. **Quantitative comparison with state-of-the-art methods on WFLW and its six subsets.** NME is reported for all subsets. The **best** and **second best** results are highlighted. The † symbol represents the results we reproduced.

of landmarks occluded. Every landmark is accompanied by an additional label indicating whether the landmark is occluded or not. However, we do not use the occlusion label in the experiments.

300W is commonly used in facial landmark detection, comprising 3148 training images and 689 testing images, with 68 landmarks per image. We also adopt the common setting on 300W, splitting the test set into the common subset of 554 images and the challenging subset of 135 images.

Data Augmentation. We employ various data augmentation techniques in our experiments. For the quantized heatmap generator and ORFormer, we start by cropping the face region from the original image and resizing it to 64×64 pixels. Subsequently, we apply random horizontal flipping (50%), random grayscale (50%), random rotation ($\pm 30^\circ$), random translation ($\pm 4\%$), and random scaling ($\pm 5\%$). Additionally, to enhance ORFormer’s ability to handle occlusions, we add an extra random occlusion to every image.

For the landmark detection model, we resize the images to 256×256 pixels and set the random occlusion probability to 40%, with other augmentation techniques kept.

4.2. Evaluation Metrics

Following previous works [11, 47], we employ three commonly used evaluation metrics to assess the accuracy of landmark detection: including normalized mean error (NME), failure rate (FR), and area under curve (AUC). For WFLW and 300W, inter-ocular NME is used, while for COFW, inter-pupil NME is used. For FR and AUC, the threshold is set to 10% for all datasets.

4.3. Comparisons with State-of-the-Art Methods

We conduct a comprehensive comparison of our method with state-of-the-art FLD approaches. As presented in Table 1, ORFormer achieves comparable or even better results

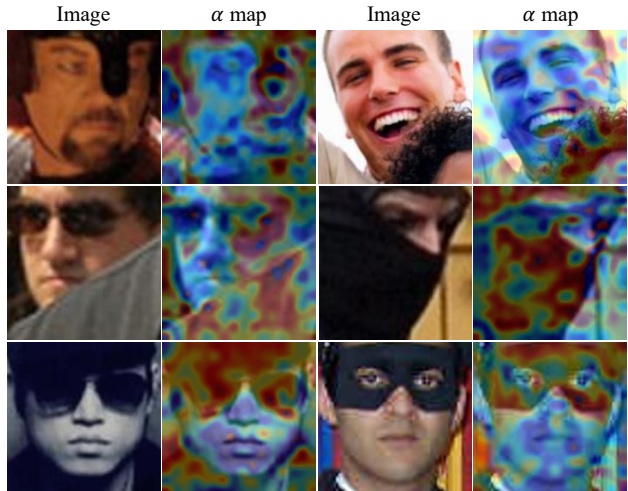


Figure 6. **Visualization of the α maps yielded by ORFormer.** Red regions indicate higher values of α , suggesting heavier feature occlusion or corruption detected by ORFormer.

on the various facial landmark datasets. Our method performs favorably against state-of-the-art methods in terms of NME and FR on WFLW, NME on COFW, and NME on the challenging subset of 300W, demonstrating the robustness of our ORFormer in challenging scenarios. For qualitative comparison, we depict the output landmarks from our approach and a strong baseline method on randomly sampled images from the test set of WFLW. We choose STAR [47] as our baseline method, which shares the same network architecture as ours. We report the results reproduced using their official repository. As shown in Figure 5, with the help of the high-quality heatmap generated from ORFormer, our approach exhibits better robustness, particularly when the face is highly occluded or in extreme head rotations, demonstrating the capability of ORFormer to generate high-quality heatmaps resilient to extreme cases.

Furthermore, we analyze the performance across six subsets on the WFLW test set to validate the effectiveness of our method. As presented in Table 2, ORFormer not only achieves state-of-the-art performance on the difficult subsets, but also excels in the occlusion, pose, illumination, and make-up subsets with large margins, demonstrating its robustness to partially non-visible facial features. The lower performance on the expression subset is attributed to the fact that it primarily consists of samples with deformed facial features.

Moreover, we visualize the output α map of ORFormer in Figure 6. Regions in red indicate heavier occlusion detected by ORFormer, while regions in blue denote less occlusion, highlighting our method’s capability to detect occluded or corrupted features.

Architecture	Full	Pose	Exp.	Ill.	Mak.	Occ.	Blur
Heatmap L2 Loss ↓							
VQVAE [34]	26.72	51.43	29.32	26.82	30.96	35.63	32.07
CodeFormer [46]	25.01 (6.4%)	49.61 (3.5%)	27.98 (4.6%)	25.22 (6.0%)	27.30 (11.8%)	32.46 (8.9%)	30.08 (6.2%)
ORFormer (Ours)	20.22 (24.3%)	36.51 (29.0%)	23.80 (18.8%)	20.83 (22.3%)	21.65 (30.1%)	25.94 (27.2%)	24.70 (23.0%)

Table 3. **Quantitative comparison for heatmap generation on WFLW.** Heatmap regression L2 loss is reported for all subsets. The relative performance gain, given in parentheses, is calculated from the baseline VQVAE [34]. Text in **bold** indicates a method gets a larger relative gain on that subset over the full set.



Figure 7. **Qualitative comparison for heatmap generation on WFLW.** GT stands for the ground-truth heatmap. For better visualization, we display the distance heatmap for VQVAE, CodeFormer, and ORFormer by computing the pixel-wise L2 distance between their output heatmaps and the GT heatmap. Brighter areas indicate higher errors. The main area of discrepancy is emphasized within an ellipse to highlight variations between the methods.

4.4. Ablation Studies

Effectiveness of ORFormer. To illustrate the performance difference of ORFormer in heatmap generation compared to baselines, we present the heatmap regression L2 loss on WFLW and its six subsets in Table 3. We denote the quantized heatmap generator described in Section 3.1 as VQVAE [34] and use it as a baseline. In addition, we denote the method that inserts a conventional ViT after the pre-trained encoder as CodeFormer [46] for comparison. While the method CodeFormer demonstrates performance gains over the baseline, ORFormer notably outperforms CodeFormer by a significant margin. Particularly in the pose, make-up, and occlusion subsets, ORFormer exhibits exceptional performance compared to the full set, highlighting its robustness to feature occlusion and corruption.

We also visualize the output heatmap in Figure 7. For ease of visual comparison, we choose the edge heatmap on the cheek and visualize the distance heatmap by computing the pixel-wise L2 distance between the output heatmap and the GT heatmap. Brighter areas indicate larger errors. In extreme cases, ORFormer can generate a better heatmap compared to other methods, showcasing the robustness to partial occlusion of ORFormer.

Method	Param. (M)	Self-Att.	Cross-Att.	Occ. Head	Occ.-Aware	L2 Loss ↓	NME ↓
VQVAE [34]	1.36					26.72	4.04
CodeFormer [46]	4.32	✓				25.13	4.00
ORFormer (Ours)	4.77	✓	✓			24.35	3.99
	4.78	✓	✓	✓		23.87	3.95
	4.78	✓	✓	✓	✓	20.22	3.86

Table 4. **Quantitative evaluation on the proposed components of ORFormer on WFLW.** The heatmap regression L2 loss and the landmark NME loss are reported.

Effectiveness of ORFormer Components. To assess the effectiveness of the components introduced in ORFormer, we analyze the heatmap regression quality using heatmap L2 loss and the landmark detection accuracy using NME loss on WFLW. While VQVAE [34] uses the quantized heatmap generator alone, CodeFormer [46] integrates a traditional ViT within the latent space of the quantized heatmap generator. Table 4 reports the performance of each additional component based on the ViT [5] architecture. We find that employing cross-attention with the proposed messenger token provides an adequate improvement over CodeFormer [46]. With the occlusion detection head, our method equips the occlusion handling ability, reflecting on the drop of the L2 regression loss. With our proposed occlusion-aware cross-attention, ORFormer effectively suppresses the feature aggregation from occluded patches, leading to a large margin in reducing the L2 loss and NME loss.

More ablation studies, the analysis of the computational complexity, and the discussion of the limitations of ORFormer can be found in the supplementary materials.

5. Conclusion

In this paper, we introduce a novel occlusion-robust transformer architecture called ORFormer, designed to detect occlusions and recover features for the occluded areas. Addressing the limitations of existing facial landmark detection (FLD) methods on difficult scenarios such as partially non-visible faces caused by occlusions, extreme lighting conditions, or extreme head rotations, ORFormer introduces new messenger tokens, which identify occluded features and recover missing details from visible observations. Through extensive ablation studies and experiments, we have demonstrated that ORFormer is able to generate high-quality heatmaps resilient to extreme cases. With the aid of ORFormer, our method performs favorably against the state-of-the-art FLD methods on challenging datasets, such as WFLW and COFW.

Acknowledgements. This work was supported in part by the National Science and Technology Council (NSTC) under grants 112-2221-E-A49-090-MY3, 111-2628-E-A49-025-MY3, 112-2634-F-006-002, and 113-2640-E-006-006. This work was funded in part by MediaTek.

6. Supplementary Materials

We provide additional implementation details, more ablation studies, the analysis of the computational complexity, and the discussion of the limitations of ORFormer in this supplementary document.

6.1. Additional Implementation Details

6.1.1 Model Training

We employ the Adam optimizer [15] along with the cosine annealing warm restart scheduler proposed by Loshchilov *et al.* [21] in all our experiments. The number of iterations for the first restart is set to 5, and the increase factor is set to 2.

The entire training process is carried out on a single NVIDIA GTX 1080 Ti with 11GB of memory. Specifically, for the quantized heatmap generator, we set the learning rate to 0.0007 with a batch size of 128. For deriving the proposed ORFormer, we use a learning rate of 0.0001 with a batch size of 64. For the landmark detection models, we set the learning rate to 0.001 with a batch size of 16.

6.1.2 Heatmap Definition

ORFormer aims to identify non-visible regions and recover missing features, enabling the generation of high-fidelity heatmaps resilient to challenging scenarios like occlusions, extreme lighting conditions, or extreme head rotations. This capability assists facial landmark detection (FLD) methods in maintaining robustness in such challenging scenarios.

To support FLD methods effectively and efficiently, we employ heatmaps on facial edges (contours) as constraints by following a related approach proposed by Wu *et al.* [40]. Utilizing edge heatmaps alone can reduce computational costs while providing sufficient information for FLD methods.

Heatmap Generation. As illustrated in Fig. 8, for a given face image $I \in \mathbb{R}^{h \times w \times 3}$ and its ground-truth landmark annotations $L = \{l_i\}_{i=0}^{N_L-1}$, we divide L into N_E subsets $L_j \subset L, j = 0, \dots, N_E - 1$ to represent the facial edges, such as the cheek and eyebrow. Here, N_L represents the number of landmarks per face, and N_E denotes the number of edges per face. Each facial edge L_j is utilized to interpolate the edge line, thereby forming the binary edge map B_j of the same size as the face image. Subsequently, a distance transform is applied to B_j , computing the nearest distance to the edge line for every pixel, resulting in the formation of the distance map M_j , which is also of the same size as the face image. Finally, we obtain the ground-truth edge heatmap \hat{H}_j used to supervise the quantized heatmap and

ORFormer by the following formula:

$$\hat{H}_j(x, y) = \begin{cases} \exp\left(-\frac{M_j(x, y)^2}{2\sigma^2}\right), & \text{if } M_j(x, y) < 3\sigma, \\ 0, & \text{otherwise.} \end{cases} \quad (12)$$

σ represents the standard deviation of the values in the distance map M_j .

Index Mapping. Our experiments are conducted on three distinct datasets: WFLW [40], COFW [3], and 300W [31]. As illustrated in Fig. 9, the number of landmarks varies across these datasets, leading to differences in the edge heatmap. Consequently, we provide the index mappings between the landmarks and the facial edges in the following.

For the **WFLW** dataset, with N_L equal to 98 and N_E equal to 15, the index mapping is given as follows:

Edge 0: [0–32]
Edge 1: [33–37]
Edge 2: [38–41, 33]
Edge 3: [42–46]
Edge 4: [46–49, 50]
Edge 5: [51–54]
Edge 6: [55–59]
Edge 7: [60–64]
Edge 8: [64–67, 60]
Edge 9: [68–72]
Edge 10: [72–75, 68]
Edge 11: [76–82]
Edge 12: [82–87, 76]
Edge 13: [88–92]
Edge 14: [92–95, 88]

For the **300W** dataset, with N_L equal to 68 and N_E equal to 13, the index mapping is given as follows:

Edge 0: [0–16]
Edge 1: [17–21]
Edge 2: [22–26]
Edge 3: [27–30]
Edge 4: [31–35]
Edge 5: [36–39]
Edge 6: [39–41, 36]
Edge 7: [42–45]
Edge 8: [45–47, 42]
Edge 9: [48–54]
Edge 10: [54–59, 48]
Edge 11: [60–64]
Edge 12: [64–67, 60]

For the **COFW** dataset, with N_L equal to 29 and N_E equal to 14, the index mapping is given as follows:

Edge 0: [0, 4, 2]
Edge 1: [2, 5, 0]

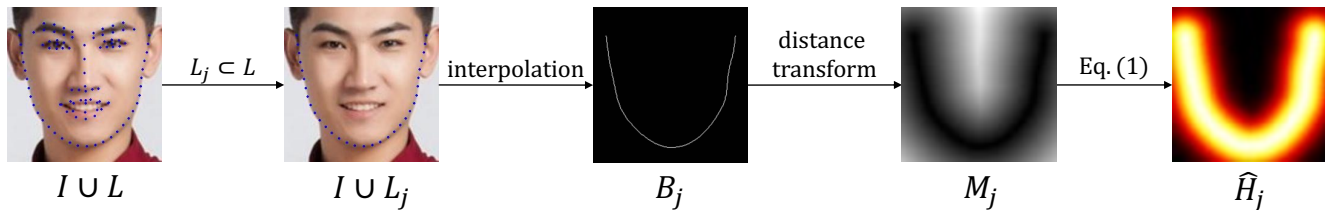


Figure 8. Generation flow of the ground-truth edge heatmap.

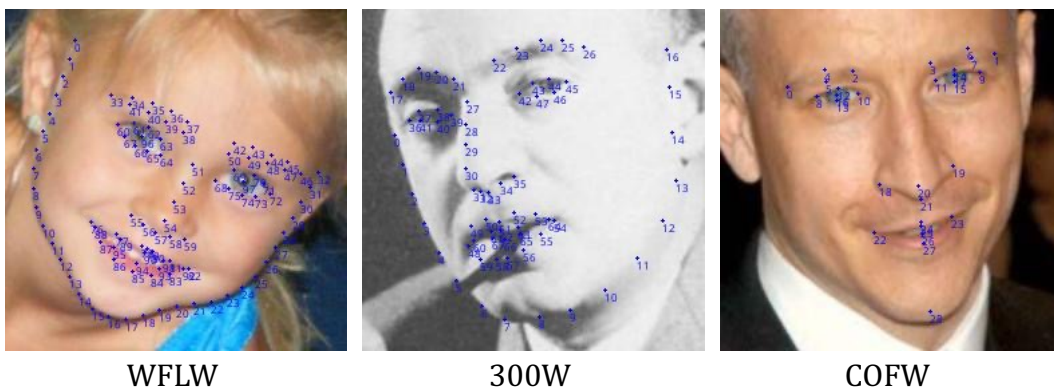


Figure 9. Visualization of the ground-truth landmarks in different datasets.

Method (Publication)	Backbone	WFLW-Full			COFW	300W (NME ₁₀ ↓)		
		NME ₁₀ ↓	FR _{10%} ↓	AUC _{10%} ↑	NME _{ip} ↓	Full	Comm.	Chal.
LAB (CVPR18) [40]	Hourglass	5.27	7.56	0.532	-	3.49	2.98	5.19
Wing (CVPR18) [7]	ResNet-50	4.99	6.00	0.550	5.44	-	-	-
HRNet (CVPR19) [32]	HRNet-W18	4.60	4.64	-	-	3.32	2.87	5.15
AWing (ICCV19) [36]	Hourglass	4.36	2.84	0.572	4.94	3.07	2.72	4.52
LUVLi (CVPR20) [16]	DU-Net	4.37	3.12	0.577	-	3.23	2.76	5.16
ADNet (ICCV21) [11]	Hourglass	4.14	2.72	0.602	4.68	2.93	2.53	4.58
PIPNet (IJCV21) [12]	ResNet-101	4.31	-	-	-	3.19	2.78	4.89
HHH (arXiv21) [17]	Hourglass	4.08	2.60	0.605	4.63	3.09	2.65	4.89
SLPT (CVPR22) [42]	HRNet-W18	4.14	2.76	0.595	4.79	3.17	2.75	4.90
RePFormer (arXiv22) [19]	ResNet-101	4.11	-	-	-	3.01	-	-
†STAR (CVPR23) [47]	Hourglass	4.03	2.32	0.611	4.62	2.90	2.52	4.46
LDEQ (CVPR23) [24]	Hourglass	3.92	2.48	0.624	-	-	-	-
ORFormer (Ours)	Hourglass	3.86	1.76	0.622	4.46	2.90	2.53	4.43

Table 5. Quantitative comparison with state-of-the-art methods on WFLW, COFW, and 300W. NME is reported for all datasets. For WFLW, FR and AUC with a threshold of 10% are included. The best and second best results are highlighted. The † symbol represents the results we reproduced.

Edge 2: [1, 6, 3]
 Edge 3: [3, 7, 1]
 Edge 4: [8, 12, 10]
 Edge 5: [10, 13, 8]
 Edge 6: [9, 14, 11]
 Edge 7: [11, 15, 9]
 Edge 8: [18, 21, 19]
 Edge 9: [20, 21]
 Edge 10: [22, 26, 23]
 Edge 11: [23, 27, 22]

Edge 12: [22, 24, 23]
 Edge 13: [23, 25, 22]

6.2. More Experiments

6.2.1 Comparisons with State-of-the-Art Methods

Due to limited space in the main paper, we provide the full experimental table here, as shown in Table 5. We also provide more samples for visualization of the output landmark, as shown in Figure 10.

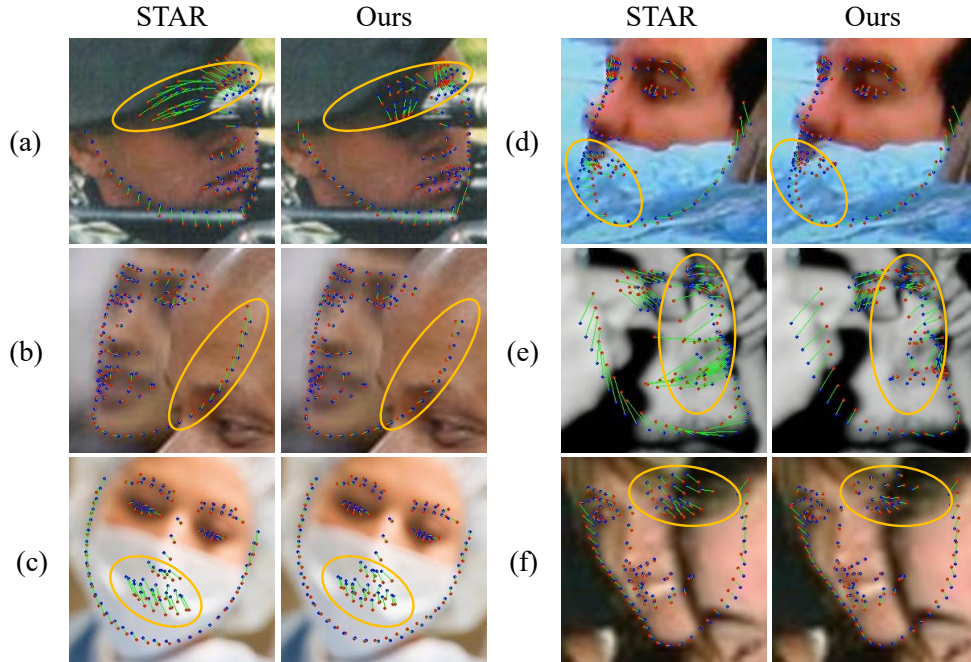


Figure 10. **Qualitative comparison with the reproduced baseline method, STAR, on extreme cases from the test set of WFLW.** The ground-truth landmarks are marked in blue, while the predicted landmarks are in red. The green lines represent the distance between the ground-truth landmarks and the predicted landmarks. Orange ellipses highlight variations between the methods in the challenging areas.

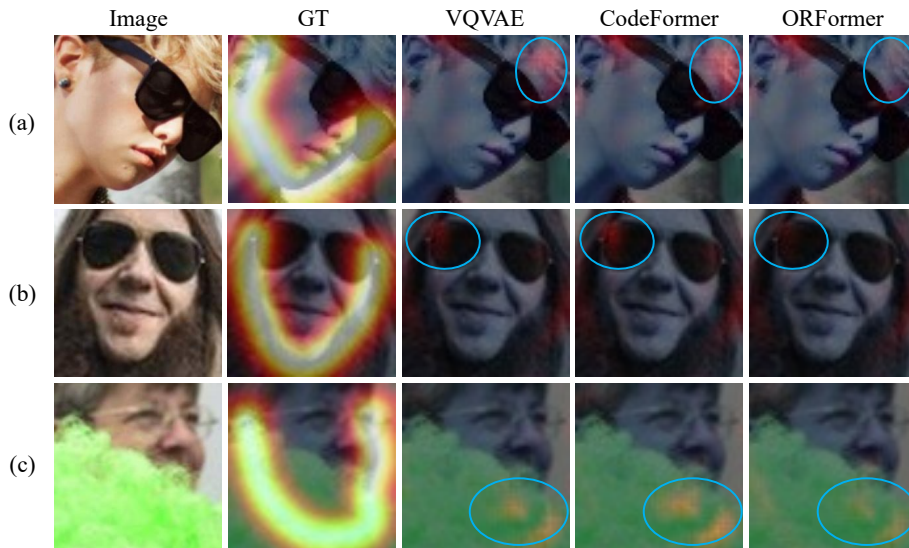


Figure 11. **Qualitative comparison for heatmap generation on WFLW.** GT stands for the ground-truth heatmap. For better visualization, we display the distance heatmap for VQVAE, CodeFormer, and ORFormer by computing the pixel-wise L2 distance between their output heatmaps and the GT heatmap. Brighter areas indicate higher errors. The main area of discrepancy is emphasized within an ellipse to highlight variations between the methods.

6.2.2 Ablation Study

Effectiveness of ORFormer . Due to limited space in the main paper, we provide more samples for visualization of

the output heatmap of ORFormer, as shown in Figure 11.

Effectiveness of ORFormer’s Heatmaps. To demonstrate the effectiveness of ORFormer for heatmaps gener-

Method	Architecture	Loss Functions		WFLW (NME↓)	
		Heatmap	Landmark	Full	Occ.
ADNet [11]	HGNet	AWing	ADL	4.14	5.06
	HGNet+ORFormer	AWing	ADL	4.06 (+1.9%)	4.94 (+2.4%)
†STAR [47]	HGNet	AWing	STAR	4.03	4.82
	HGNet+ORFormer	AWing	STAR	3.92 (+2.7%)	4.66 (+3.3%)

Table 6. **Ablation study of enabling ORFormer for landmark detection on WFLW.** NME is reported. The † symbol represents the results we reproduced. The relative performance improvement is calculated based on HGNet.

Method	Distance Function	L2 Loss ↓
ORFormer	$\text{concat}\{X - M, M - X\}$	24.86
ORFormer	$ X - M $	24.43
ORFormer	$(X - M)^2$	23.87

Table 7. **Quantitative evaluation on different designs of the distance function of ORFormer’s occlusion detection head.** X represents the image patch embedding and M represents the messenger embedding. The label Occ. Head denotes the proposed occlusion detection head. The proposed occlusion detection head is not enabled in the first-row entry. The occlusion-aware cross-attention component is not enabled here. Results highlighted in **bold** represent the best performance. The heatmap regression L2 loss is reported on WFLW.

ation for facial landmark detection, we compare it to the methods that utilize the same baseline network: ADNet [11] and STAR [47]. The results are presented in Table 6. By incorporating ORFormer’s output heatmaps as additional information to the networks, alongside the same loss functions used by ADNet and STAR, our method achieves performance gains, especially in the occlusion subset, showing the effectiveness of ORFormer’s heatmap to existing FLD methods.

Occlusion Detection Head. As mentioned in the paper, we incorporate an occlusion detection head in our proposed ORFormer to identify occluded patches by evaluating the dissimilarity between the image patch embedding X^{l+1} and the messenger embedding M^{l+1} . The patch-specific occlusion map $\alpha_k^{l+1} = \{\alpha_k^{l+1}\}_{k=0}^{m \times n - 1}$ is obtained via

$$\alpha_k^{l+1} = \sigma(W^{l+1} \cdot \text{dist}(X_k^{l+1}, M_k^{l+1})), \quad (13)$$

where $\text{dist}(\cdot, \cdot)$ calculates the element-wise squared difference between the two embeddings, W^{l+1} represents a fully connected layer that transforms the embedding returned by dist into a scalar, and $\sigma(\cdot)$ is the sigmoid function ensuring α_k^{l+1} ranges between 0 and 1.

To explore the difference between designs of distance functions, we compare the heatmap regression quality us-

Method	W ’s Design	L2 Loss ↓
ORFormer	5×5 conv.	24.26
ORFormer	3×3 conv.	24.05
ORFormer	Fully connected layer	23.87

Table 8. **Quantitative evaluation with different filter sizes of W in ORFormer’s occlusion detection head.** The occlusion-aware cross-attention component is not enabled here. Results highlighted in **bold** represent the best performance. The heatmap regression L2 loss is reported on WFLW.

Method	Integration	Pre-trained Weights	Trainable Part	NME _{io} ↓
ORFormer				4.03
ORFormer	✓	✓	Conv.	4.01
ORFormer	✓	✓	All	3.94
ORFormer	✓		All	3.86

Table 9. **Quantitative evaluation of different integration methods of ORFormer with Existing FLD Methods** The Conv. label indicates the 1×1 CNN block used to merge the heatmap generated by ORFormer with the feature maps of existing FLD methods. The first row entry represent reproducing STAR [47] without the integration with ORFormer. Results highlighted in **bold** represent the best performance. The landmark detection NME loss is reported on WFLW.

ing L2 loss with various designs of the distance function, as shown in Table 7. We observe that employing the squared difference as the distance function in the occlusion detection head yields the best performance. This improvement can be attributed to the squared difference function’s capability to impose a larger penalty when there is a large disparity between the image patch embedding X^{l+1} and the messenger embedding M^{l+1} , while still enabling the gradient to propagate continuously.

To explore incorporating more information into ORFormer during occlusion detection, we compare the heatmap regression quality using L2 loss with different filter sizes of W in Eq. 13, as shown in Table 8. For the convolutional layer, we reshape the embedding back to $\mathbb{R}^{m \times n \times d}$ before applying the convolution operation. In contrast, for the fully connected layer, we pass the embedding one by one, equivalent to applying a 1×1 convolutional layer in the shape of $\mathbb{R}^{m \times n \times d}$. Using a larger filter size for the convolutional layer allows the occlusion detection head to consider more information from neighboring embeddings when detecting occlusion. However, we observe that using a fully connected layer performs best. We believe this is because ORFormer operates in the latent space of the quantized heatmap generator, considering one single embedding in this latent space can provide an appropriate receptive field for occlusion detection in human faces.

Method	Architecture	Loss Functions		WFLW (NME \downarrow)	
		Heatmap	Landmark	Full	Occ.
ADNet [11]	HGNet	AWing	ADL	4.14	5.06
Ours	HGNet+ORFormer	AWing	ADL	4.06	4.94
†STAR [47]	HGNet	AWing	STAR	4.03	4.82
Ours	HGNet+ORFormer	AWing	STAR	3.92	4.66
Ours	HGNet+ORFormer	L2	NME	3.86	4.57

Table 10. **Quantitative evaluation of different loss functions of the integration of ORFormer with Existing FLD Methods.** All methods utilize the same backbone. Loss functions highlighted in blue represent the proposed approaches of that work. Results highlighted in bold represent the best performance. The landmark detection NME loss is reported on the WFLW dataset. The † symbol represents the results we reproduced.

Integration with FLD Methods. With our ORFormer for occlusion detection and feature recovery, the quantized heatmap generator can produce high-quality heatmaps. We integrate these heatmaps as additional structural guidance into existing FLD methods [11, 47]. Specifically, we concatenate the heatmaps with the feature maps in the early stage and merge them with a single lightweight 1×1 CNN block.

Way of Integration. To explore the best strategy of integrating the heatmap produced by ORFormer into existing FLD methods, we compare the landmark detection accuracy using NME loss with different integration strategies. The results are shown in Table 9. The pre-trained weights are from reproducing STAR [47] with an NME of 4.03. We find that by only fine-tuning the lightweight CNN block, we gain little performance with the help of ORFormer’s heatmap. However, if we fine-tune the entire network or train the entire network from scratch without using pre-trained weights, we can achieve larger performance gains.

Loss Function. We also explore alternative choices of the loss function for model integration. As shown in Table 10, by integrating the output heatmaps of ORFormer into existing FLD methods [11, 47] and using the same loss functions, our approach achieves improved performance. Moreover, we obtain the best result using a simple loss function such as L2 loss for heatmap supervision and NME loss for landmark supervision. We believe this is because our heatmap definition differs from ADNet and STAR. While our heatmap is suitable for L2 loss, their heatmap is defined for the use of their proposed specific loss functions.

6.2.3 Computational Complexity of ORFormer

In Table 11, we show the numbers of trainable parameters of ORFormer. Compared to the conventional ViT, ORFormer

Method	Param. (M)	Self-Att.	Cross-Att.	Occ. Head	Occ.-Aware	L2 Loss \downarrow	NME \downarrow
VQVAE [34]	1.36					26.72	4.04
CodeFormer [46]	4.32	✓				25.13	4.00
ORFormer (Ours)	4.77	✓	✓			24.35	3.99
	4.78	✓	✓	✓		23.87	3.95
	4.78	✓	✓	✓	✓	20.22	3.86

Table 11. **Quantitative evaluation on the proposed components of ORFormer on WFLW.** The heatmap regression L2 loss and he landmark NME loss are reported.

Method	Architecture	Param. (M)	Mult-Add (G)	Infer. Time (ms)	NME \downarrow
†STAR [47]	4-stack HGNet	17	17.4	45	4.03
†STAR [47]	5-stack HGNet	21.5	21.5	63	3.98
Ours	4-stack HGNet+ORFormer	21.8	17.9	53	3.86
		(+1.4%)	(-20.6%)	(-15.9%)	

Table 12. **Ablation study of computation complexity vs NME on WFLW.** HGNet represents the hourglass network. The relative increase/improvement is calculated based on 5-stack HGNet. The † symbol represents the results we reproduced. The inference time is tested on a single NVIDIA GTX 1080 Ti.

enhances ViT to handle occlusions with minimal overhead, with about 10% more trainable parameters.

Even though ORFormer doubles the token count of a regular ViT, the patch token and messenger token compute attention scores separately, affecting the computational complexity linearly and thus minimally impacting the inference time. In Table 12, we integrate our proposed ORFormer into the state-of-the-art baseline, STAR [47], a 4-stack Hourglass network. For fair comparison, we augment the baseline network with one additional stack to align the number of trainable parameters. Our method performs favorably against this augmented baseline with comparable trainable parameters, 20.6% fewer mult-add operations, and 15.9% less inference time, showing the advantage of ORFormer.

6.2.4 Limitations

The first limitation is that ORFormer is particularly effective at handling partially non-visible facial features but struggles with partially deformed facial features. The second limitation is that although ORFormer yields features robust to occlusion, the capability of our method relies on a well-trained quantized heatmap generator, which limits its applicability to tasks related to heatmap generation. In future research, we plan to explore ways to enable ORFormer to handle partially deformed facial features and extend ORFormer to serve as a general feature extractor for various computer vision tasks, where partial occlusions detection and feature recovery are essential, maximizing its impact in the field of computer vision.

References

- [1] Emad Barsoum, Cha Zhang, Cristian Canton Ferrer, and Zhengyou Zhang. Training deep networks for facial expression recognition with crowd-sourced label distribution. In *ACM international conference on multimodal interaction*, 2016. 1
- [2] Adrian Bulat, Enrique Sanchez, and Georgios Tzimiropoulos. Subpixel heatmap regression for facial landmark localization. *arXiv preprint arXiv:2111.02360*, 2021. 2
- [3] Xavier P Burgos-Artizzu, Pietro Perona, and Piotr Dollár. Robust face landmark estimation under occlusion. In *ICCV*, 2013. 1, 3, 6, 9
- [4] Xuanyi Dong, Shoou-I Yu, Xinshuo Weng, Shih-En Wei, Yi Yang, and Yaser Sheikh. Supervision-by-registration: An unsupervised approach to improve the precision of facial landmark detectors. In *CVPR*, 2018. 2
- [5] Alexey Dosovitskiy, Lucas Beyer, Alexander Kolesnikov, Dirk Weissenborn, Xiaohua Zhai, Thomas Unterthiner, Mostafa Dehghani, Matthias Minderer, Georg Heigold, Sylvain Gelly, et al. An image is worth 16x16 words: Transformers for image recognition at scale. *arXiv preprint arXiv:2010.11929*, 2020. 1, 3, 8
- [6] Patrick Esser, Robin Rombach, and Bjorn Ommer. Taming transformers for high-resolution image synthesis. In *CVPR*, 2021. 3
- [7] Zhen-Hua Feng, Josef Kittler, Muhammad Awais, Patrik Huber, and Xiao-Jun Wu. Wing loss for robust facial landmark localisation with convolutional neural networks. In *CVPR*, 2018. 1, 2, 6, 7, 10
- [8] Xiaojie Guo, Siyuan Li, Jinke Yu, Jiawan Zhang, Jiayi Ma, Lin Ma, Wei Liu, and Haibin Ling. Pflid: A practical facial landmark detector. *arXiv preprint arXiv:1902.10859*, 2019. 1, 2
- [9] Kaiming He, Xiangyu Zhang, Shaoqing Ren, and Jian Sun. Deep residual learning for image recognition. In *CVPR*, 2016. 5
- [10] Thorsten Hempel, Ahmed A Abdelrahman, and Ayoub Al-Hamadi. 6d rotation representation for unconstrained head pose estimation. In *ICIP*, 2022. 1
- [11] Yangyu Huang, Hao Yang, Chong Li, Jongyoo Kim, and Fangyun Wei. Adnet: Leveraging error-bias towards normal direction in face alignment. In *ICCV*, 2021. 1, 2, 6, 7, 10, 12, 13
- [12] Haibo Jin, Shengcai Liao, and Ling Shao. Pixel-in-pixel net: Towards efficient facial landmark detection in the wild. *IJCV*, 2021. 2, 6, 7, 10
- [13] Aniwat Juhong and Chuchart Pintavirooj. Face recognition based on facial landmark detection. In *Biomedical Engineering International Conference*, 2017. 1
- [14] Dongwoo Kang and Lin Ma. Real-time eye tracking for bare and sunglasses-wearing faces for augmented reality 3d head-up displays. *IEEE Access*, 2021. 1
- [15] Diederik P Kingma and Jimmy Ba. Adam: A method for stochastic optimization. *arXiv preprint arXiv:1412.6980*, 2014. 9
- [16] Abhinav Kumar, Tim K Marks, Wenxuan Mou, Ye Wang, Michael Jones, Anoop Cherian, Toshiaki Koike-Akino, Xiaoming Liu, and Chen Feng. Luvli face alignment: Estimating landmarks' location, uncertainty, and visibility likelihood. In *CVPR*, 2020. 2, 6, 10
- [17] Xing Lan, Qinghao Hu, Qiang Chen, Jian Xue, and Jian Cheng. Hih: Towards more accurate face alignment via heatmap in heatmap. *arXiv preprint arXiv:2104.03100*, 2021. 6, 7, 10
- [18] Hui Li, Zidong Guo, Seon-Min Rhee, Seungju Han, and Jae-Joon Han. Towards accurate facial landmark detection via cascaded transformers. In *CVPR*, 2022. 2
- [19] Jinpeng Li, Haibo Jin, Shengcai Liao, Ling Shao, and Pheng-Ann Heng. Repformer: Refinement pyramid transformer for robust facial landmark detection. In *IJCAI*, 2022. 2, 6, 7, 10
- [20] Yaokun Li, Guang Tan, and Chao Gou. Cascaded iterative transformer for jointly predicting facial landmark, occlusion probability and head pose. *IJCV*, 2024. 2
- [21] Ilya Loshchilov and Frank Hutter. Sgdr: Stochastic gradient descent with warm restarts. *arXiv preprint arXiv:1608.03983*, 2016. 9
- [22] Daniel Merget, Matthias Rock, and Gerhard Rigoll. Robust facial landmark detection via a fully-convolutional local-global context network. In *CVPR*, 2018. 3
- [23] Xin Miao, Xiantong Zhen, Xianglong Liu, Cheng Deng, Vasilis Athitsos, and Heng Huang. Direct shape regression networks for end-to-end face alignment. In *CVPR*, 2018. 2
- [24] Paul Micaelli, Arash Vahdat, Hongxu Yin, Jan Kautz, and Pavlo Molchanov. Recurrence without recurrence: Stable video landmark detection with deep equilibrium models. In *CVPR*, 2023. 2, 6, 7, 10
- [25] Ali Mollahosseini, David Chan, and Mohammad H Mahoor. Going deeper in facial expression recognition using deep neural networks. In *WACV*, 2016. 1
- [26] Alejandro Newell, Kaiyu Yang, and Jia Deng. Stacked hour-glass networks for human pose estimation. In *ECCV*, 2016. 2, 6
- [27] Aiden Nibali, Zhen He, Stuart Morgan, and Luke Prendergast. Numerical coordinate regression with convolutional neural networks. *arXiv preprint arXiv:1801.07372*, 2018. 2
- [28] JoonKyu Park, Yeonguk Oh, Gyeongsik Moon, Hongsuk Choi, and Kyoung Mu Lee. Handocnet: Occlusion-robust 3d hand mesh estimation network. In *CVPR*, 2022. 3
- [29] Omkar Parkhi, Andrea Vedaldi, and Andrew Zisserman. Deep face recognition. In *BMVC*, 2015. 1
- [30] Olaf Ronneberger, Philipp Fischer, and Thomas Brox. U-net: Convolutional networks for biomedical image segmentation. In *Medical Image Computing and Computer-Assisted Intervention*, 2015. 2
- [31] Christos Sagonas, Georgios Tzimiropoulos, Stefanos Zafeiriou, and Maja Pantic. 300 faces in-the-wild challenge: The first facial landmark localization challenge. In *ICCV workshops*, 2013. 6, 9
- [32] Ke Sun, Bin Xiao, Dong Liu, and Jingdong Wang. Deep high-resolution representation learning for human pose estimation. In *CVPR*, 2019. 2, 6, 7, 10

- [33] Roberto Valle, José M Buenaposada, and Luis Baumela. Multi-task head pose estimation in-the-wild. *PAMI*, 2020. [1](#)
- [34] Aaron Van Den Oord, Oriol Vinyals, et al. Neural discrete representation learning. In *NeurIPS*, 2017. [3](#), [4](#), [8](#), [13](#)
- [35] Ashish Vaswani, Noam Shazeer, Niki Parmar, Jakob Uszkoreit, Llion Jones, Aidan N Gomez, Łukasz Kaiser, and Illia Polosukhin. Attention is all you need. In *NeurIPS*, 2017. [2](#), [3](#)
- [36] Xinyao Wang, Liefeng Bo, and Li Fuxin. Adaptive wing loss for robust face alignment via heatmap regression. In *ICCV*, 2019. [1](#), [2](#), [6](#), [7](#), [10](#)
- [37] Ukrit Watchareeruetai, Benjaphan Sommana, Sanjana Jain, Pavit Noinongyao, Ankush Ganguly, Aubin Samacoits, Samuel WF Earp, and Nakarin Sritrakool. Lotr: face landmark localization using localization transformer. *IEEE Access*, 2022. [2](#)
- [38] Wei Wei, Edmond SL Ho, Kevin D McCay, Robertas Damaševičius, Rytis Maskeliūnas, and Anna Esposito. Assessing facial symmetry and attractiveness using augmented reality. *Pattern Analysis and Applications*, 2021. [1](#)
- [39] Wenyang Wu, Yici Cai, and Qiang Zhou. Transmarker: a pure vision transformer for facial landmark detection. In *ICPR*, 2022. [2](#)
- [40] Wayne Wu, Chen Qian, Shuo Yang, Quan Wang, Yici Cai, and Qiang Zhou. Look at boundary: A boundary-aware face alignment algorithm. In *CVPR*, 2018. [1](#), [2](#), [4](#), [6](#), [7](#), [9](#), [10](#)
- [41] Yue Wu and Qiang Ji. Robust facial landmark detection under significant head poses and occlusion. In *ICCV*, 2015. [2](#)
- [42] Jiahao Xia, Weiwei Qu, Wenjian Huang, Jianguo Zhang, Xi Wang, and Min Xu. Sparse local patch transformer for robust face alignment and landmarks inherent relation learning. In *CVPR*, 2022. [1](#), [2](#), [6](#), [7](#), [10](#)
- [43] Boqiang Xu, Lingxiao He, Jian Liang, and Zhenan Sun. Learning feature recovery transformer for occluded person re-identification. *TIP*, 2022. [3](#)
- [44] Zhanpeng Zhang, Ping Luo, Chen Change Loy, and Xiaoou Tang. Facial landmark detection by deep multi-task learning. In *ECCV*, 2014. [2](#)
- [45] Erjin Zhou, Haoqiang Fan, Zhimin Cao, Yuning Jiang, and Qi Yin. Extensive facial landmark localization with coarse-to-fine convolutional network cascade. In *ICCV workshops*, 2013. [2](#)
- [46] Shangchen Zhou, Kelvin Chan, Chongyi Li, and Chen Change Loy. Towards robust blind face restoration with codebook lookup transformer. In *NeurIPS*, 2022. [3](#), [4](#), [8](#), [13](#)
- [47] Zhenglin Zhou, Huaxia Li, Hong Liu, Nanyang Wang, Gang Yu, and Rongrong Ji. Star loss: Reducing semantic ambiguity in facial landmark detection. In *CVPR*, 2023. [1](#), [2](#), [6](#), [7](#), [10](#), [12](#), [13](#)
- [48] Congcong Zhu, Xintong Wan, Shaorong Xie, Xiaoqiang Li, and Yinzheng Gu. Occlusion-robust face alignment using a viewpoint-invariant hierarchical network architecture. In *CVPR*, 2022. [3](#)
- [49] Meilu Zhu, Daming Shi, Mingjie Zheng, and Muhammad Sadiq. Robust facial landmark detection via occlusion-adaptive deep networks. In *CVPR*, 2019. [3](#)